Xe^+ Ion Transport in the Crossed-Field Discharge of a 5-kW-Class Hall Effect Thruster

Stéphane Mazouffre, Damien Gawron, Vladimir Kulaev, and Nader Sadeghi

***Abstract*—The velocity-distribution function (VDF) of metastable Xe^+ ions was measured along the channel axis of the 5-kW-class PPSX000 Hall effect thruster by means of laser-induced fluorescence spectroscopy at 834.72 nm for various voltages, magnetic fields, and mass flow rates. Axial-velocity and dispersion profiles are compared to on-axis profiles obtained with the 1.5-kW-class PPS100 thruster. Outcomes of the comparison are threefold: 1) The broadening of the VDF across the region of strong magnetic field is a general feature for Hall thrusters. It originates in the overlap between ionization and acceleration layers. The kinetic-energy dispersion increases with the discharge voltage; it reaches up to 200 eV at 700 V. 2) Most of the acceleration potential is localized outside the thruster channel whatever the thruster size and operating conditions. The electric field moves upstream when the applied voltage is ramped up, i.e., the fraction of potential inside the channel increases with the voltage. On the contrary, the electric field is shifted downstream when the gas flow rate increases. The magnetic field has a little impact on the potential distribution. 3) A nonnegligible amount of very fast (kinetic energy higher than the applied potential) and very slow Xe^+ ions are always observed. Such ions may find their origin in space and temporal oscillations of the electric field as suggested by numerical simulations carried out with both kinetic and hybrid models.**

***Index Terms*—Electric propulsion, Hall effect thruster (HET), ion velocity-distribution function (VDF), laser spectroscopy.**

I. Introduction

HALL effect thrusters (HETs), also called stationary plasma thrusters or closed electron drift thrusters, are advanced electric propulsion devices for spacecrafts that use a cross-field electric discharge to ionize and accelerate a propellant gas [1], [2]. HETs offer a high performance level in the viewpoint of propellant consumption and efficiency as well as interesting features in terms of lifetime, flexibility, and thrust-specific impulse couple, making them attractive for maneuvers that requires a large velocity increment. Currently, HETs are employed for missions like geostationary satellite orbit correction and station keeping. The additional utilization of high-power Hall thrusters for orbit transfer would also offer significant benefits in terms of launch mass, payload mass, and operational life. Besides, the success of the SMART-1 Moon flyby solar-powered mission of the European Space Agency has demonstrated that HETs are good candidates to be used as the primary propulsion engine for space probes during deep-space journeys [3].

Manuscript received November 20, 2007; revised February 12, 2008. Current version published November 14, 2008. This work is carried out in the frame of the French joint-research program CNRS/CNES/Snecma/Universités 2759 "Propulsion Spatiale à Plasma."

S. Mazouffre, D. Gawron, and V. Kulaev are with the CARE Institute, CNRS, 45071 Orléans, France (e-mail: stephane.mazouffre@cnrs-orleans.fr).

N. Sadeghi is with the LSP, Joseph Fourier University, CNRS, 38402 Saint Martin d'Hères, France.

Color versions of one or more of the figures in this paper are available online at http://ieeexplore.ieee.org.

Digital Object Identifier 10.1109/TPS.2008.2004240

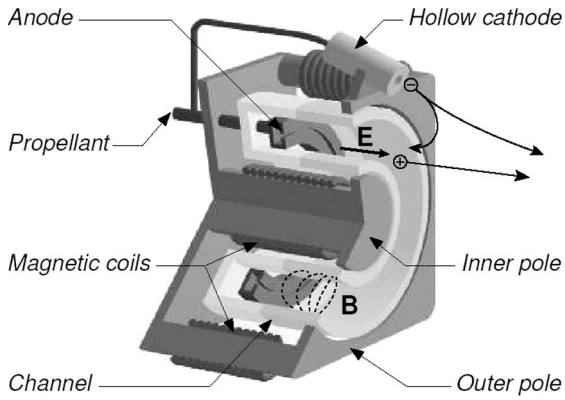

Fig. 1. Schematic of a HET.

The basic physics of a HET consists of a magnetic barrier in a low-pressure dc discharge generated between an external hollow cathode and an anode located at the upstream end of a coaxial annular dielectric channel that confines the discharge [4]–[6]. Xenon is generally used as a propellant gas for its specific properties in terms of high atomic mass and low ionization energy. A set of solenoids provides a radially directed magnetic field $\mathbf{B}$ of which the strength is maximum in the vicinity of the channel exhaust. The magnetic field is chosen strong enough to make the electron Larmor radius much smaller than the discharge-chamber length but weak enough not to affect ion trajectories. The electric potential drop is mostly concentrated in the final section of the channel, owing to the low electron axial mobility in this restricted area. The corresponding induced local axial electric field $\mathbf{E}$ has two main effects. First, it drives a high electron azimuthal drift, the so-called Hall current, that is responsible for the efficient ionization of the supplied gas. Second, it accelerates out of the channel the created ions, which generates thrust. The ion beam is neutralized by a fraction of electrons emitted from the hollow cathode. A typical HET design is shown in Fig. 1. When operating near 5 kW, a HET ejects ions at about 30 km/s, and it generates either 300 mN of thrust or 2500 s of specific impulse with an efficiency in excess of 50% [7].

Several physical mechanisms that govern the behavior of the low-pressure $\mathbf{E} \times \mathbf{B}$ discharge of a HET are still ill-understood. Among others, one can cite the anomalous electron diffusion across the magnetic barrier, the plasma–wall interactions, the plasma-sheath properties, the coupling between ionization and

acceleration processes, as well as the energy transfer and the energy losses. This lack of knowledge is a limiting factor to optimize existing HETs over a broad range of input power, to define novel and more efficient thruster architectures, and to develop predictive modeling tools. As we will see, the fine examination of ion-transport phenomena in a HET is a powerful way to improve our understanding about the physics at work in this specific type of plasma source. As Xe^+ ions are not magnetized, by measuring the ion velocity, it is possible to reconstruct the electric-field distribution, the latter being linked to the magnetic-field map and the anomalous electron diffusion. A measurement of the ion velocity spread provides valuable information about the overlapping between the ionization and the acceleration layers and the coupling between thrust and specific-impulse generation. The observation of fast ions of which the kinetic energy is higher than the applied potential energy is an important feature of a HET plasma that reveals a peculiar dynamics of the electric field. Finally, the ion-flow characteristics by themselves are of relevance, since they result from the overall HET plasma properties.

Laser-induced fluorescence (LIF) spectroscopy has often been used in the past few years to measure the velocity of metastable ions in the plasma of a Hall thruster [8]–[11]. In this paper, we present spatially resolved measurements of the Xe^+ ion velocity-distribution function (VDF) in the discharge chamber and in the plasma plume of the 5-kW-class PPSX000 HET performed by means of LIF spectroscopy in the near-infrared. Ion VDFs were measured parallel to the thruster axis, i.e., in the electric-field direction, for a broad range of applied discharge voltage (300–700 V) and magnetic-field strength (100–160 G). The effect of the xenon gas flow rate upon the ion-flow properties was also investigated. On-axis profiles of the time-averaged ion axial velocity, kinetic-energy-dispersion profiles, and electric-field distributions are presented, discussed, and compared to the ones obtained with the 1.5-kW-class PPS100 thruster. Furthermore, experimental results are compared to outcomes of numerical simulations carried out with particle-in-cell (PIC) and hybrid codes.

II. Experimental Arrangement

A. Metastable Xe^+ Ion-Detection Scheme

LIF spectroscopy is a nonintrusive diagnostic tool that enables to determine the velocity of probed particles along the laser-beam direction by measuring the Doppler shift of absorbed photons. The transition used in this paper is the $5d^2F_{7/2} \rightarrow 6p^2D^{\circ}_{5/2}$ at $\lambda_{\mathrm{air}} = 834.7233$ nm, which has been chosen due to a large population in the $5d^2F_{7/2}$ metastable state of Xe^+ ion and due to the favorable branching ratio of the $\lambda_{\mathrm{air}} = 541.915$ nm line originating from its upper state, which allows nonresonant LIF. Measuring the frequency ν at which the laser-beam energy is absorbed permits us to determine the ion Doppler shift. Therefore, it is possible to calculate the ion-velocity component corresponding to the laser-beam direction by using the following formula:

$$\Delta\nu = \nu - \nu_0 = \frac{1}{2\pi}\mathbf{k}\cdot\mathbf{v} \tag{1}$$

where $\Delta\nu$ is the Doppler shift, $\mathbf{k}$ is the laser-beam wave vector, and $\mathbf{v}$ is the ion velocity vector. Under our conditions, vectors $\mathbf{k}$ and $\mathbf{v}$ are parallel. Equation (1) then reads

$$v_x = c\frac{\nu - \nu_0}{\nu} \approx c\frac{\nu - \nu_0}{\nu_0} \tag{2}$$

where c is the speed of light in vacuum. In (1) and (2), ν_0 is the studied transition unshifted frequency, and ν is the laser frequency. We have made our own precise measurement of the absolute value of ν_0 in a low-pressure stationary xenon RF discharge: $\nu_0 = 3.59050 \times 10^{14}$ Hz $\pm$ 50 MHz.[1]

The width of a measured VDF is typically above 3000 m/s in the region of strong magnetic field as we will see. It exits nine stable isotopes of xenon, two of them having a nonzero nuclear spin. As a consequence, the studied transition is made up of 19 components. The most intense components form a distribution whose width is around 500 m/s at 300 K. The hyperfine and isotopic structure is therefore neglected. In addition, the velocity dispersions due to the isotope mass ($\Delta v \approx 580$ m/s at 700 V) and the Zeeman splitting ($\Delta v < 800$ m/s) are not accounted for as they are small with respect to the observed ion VDF width.

B. Optical Bench and Detection Branch

The LIF optical bench is extensively described in [10] and [11]. The laser beam used to excite Xe^+ metastable ions is produced by an amplified tunable single-mode external-cavity laser diode (MOPA) that can deliver up to 700 mW of power in the near-IR spectral domain. The laser remains mode-hop free over a frequency-tuning range of more than 10 GHz. The spectral width of the laser-beam profile is about 1 MHz. Behind the tapered amplifier, the laser beam passes through a Faraday isolator to prevent optical feedback into the laser cavity. The wavelength is accurately measured by means of a calibrated wavemeter whose absolute accuracy is better than 100 MHz, which corresponds to 90 m/s. A plane-scanning Fabry–Pérot interferometer with a 1.29-GHz free spectral range is used to real-time check the quality of the laser mode. The power of the beam is also continuously monitored. The primary laser beam is modulated by a mechanical chopper before being coupled into a 60-m-long multimode optical fiber of 50-μm core diameter. The fiber allows us to carry the beam into the vacuum chamber of the PIVOINE-2g ground-test facility [7]. The fiber output is located behind the thruster. Collimation optics is used to form a narrow beam that passes through a 1.5 mm in diameter hole located at the back of the PPSX000 thruster. The laser beam propagates parallel to the channel axis in the direction of the ion flow. About 3 mW of light power are deposited into the detection volume.

A detection branch made of a 40-mm focal length, which focuses the fluorescence light onto a 200-μm core diameter optical fiber, is mounted onto a travel stage perpendicular to the channel axis. The magnification ratio is one, meaning that the spatial resolution is 200 μm in axial direction. A 16 mm

[1] $\lambda_0 = (834.9527 \pm 0.0001)$ nm in vacuum.

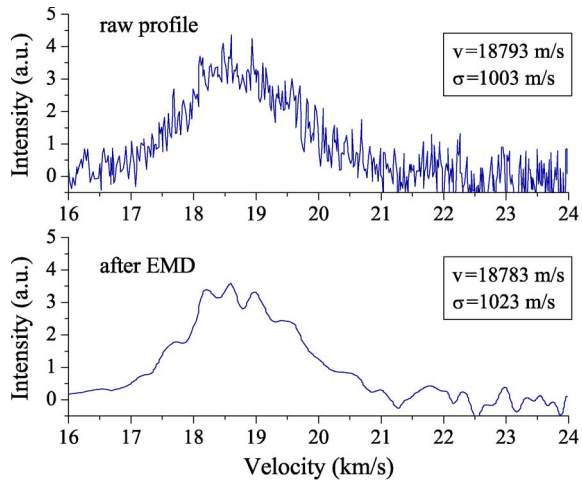

Fig. 2. Example of a Xe^+ ion VDF obtained by LIF. Top: Raw distribution for 500 V, 15 A, and 6 mg/s at $x = 5$ mm. Bottom: Distribution after smoothing by way of the EMD method.

in length slit was made in the channel dielectric outer wall in order to carry out measurements inside the channel. The collection system allows us to probe an area stretching from 16 mm into the channel up to 50 mm outside. The LIF light transported by the 200-μm fiber is focused onto the entrance slit of a 20-cm focal-length monochromator that isolates the 541.9-nm line from the rest of the spectrum. A photomultiplier tube serves as a light detector. A lock-in amplifier operating at the chopper frequency (200–400 Hz) is used to discriminate the fluorescence light from the intrinsic plasma emission. Scanning of the MOPA cavity, data acquisition, and laser-wavelength monitoring are computer controlled.

III. Analysis of Recorded VDF

A. Smoothing Procedure

Instead of classical smoothing technique like averaging, we used the empirical-mode-decomposition (EMD) method to reduce the noise level of the measured fluorescence spectra. In short, the EMD is a self-adaptive-decomposition method that allows us to split up any data series into its individual characteristic oscillations, so-called intrinsic-mode functions, each mode having its own frequency scale and energy content. When applying EMD to an ion VDF measured by LIF, one typically obtains six to seven modes and a residual. Data smoothing is then realized by removing the high-frequency modes. The advantage of this method is that it permits us to easily separate electronic- and plasma-induced noises (HF part of the signal) from the fluorescence signal (LF part of the signal). However, the problem of the origin of midfrequency part of the signal remains, meaning that data treatment must be done with care. For all results presented in this paper, the first two modes with highest frequencies have been removed. An example of data-smoothing outcome is shown in Fig. 2. Naturally, the EMD smoothing technique shall not deform the original VDF. The level of disturbance can be assessed from a comparison between raw and smoothed profiles. For the mean velocity, the gap stays below ± 100 m/s whatever the x location. For the velocity dispersion, the difference is most of the time below 5%.

A statistical analysis of series of measurements performed with the same set of parameters gives the experimental error bars: $\pm 5\%$, for the mean velocity, and $\pm 20\%$, for the velocity dispersion, respectively.

B. Quantities to be Studied

Instead of comparing time-averaged ion VDF to one another, it is much wiser to analyze statistical quantities directly inferred from the moments of the VDF.

1) The mean ion velocity $\overline{v}$ is obtained from the first-order moment of the velocity distribution.
2) The velocity spread or dispersion σ corresponds to the standard deviation; it is computed from the second-order moment of the distribution.

The following three other quantities are used.

1) The so-called maximum ion velocity $v_{\max}$; it corresponds to the velocity for which the amplitude of the distribution drops down to 10% of its maximum value on the high-velocity side [10], [11]. The arbitrary 10% factor is chosen to warrant an unambiguous definition of $v_{\max}$ as the poor S/N ratio enables us to accurately determine the true maximum velocity from the measured VDFs. In like manner, one can define a minimum velocity $v_{\min}$, considering the low-velocity wing of the distribution.
2) The p parameter which is another way to define the velocity dispersion. It reads

$$p = 2\sqrt{2\,Ln(2)} \times \sigma \approx 2.335 \times \sigma \tag{3}$$

where σ is the standard deviation. The quantity p is equal to the FWHM in the case of a Gaussian distribution. In the remainder of this paper, the p parameter is used as a value of the dispersion.
3) It is of interest to calculate the spread in kinetic energy ΔE_k in order to compare it with the applied potential energy $e\,U_d$, where e is the elementary charge. The spread in E_k is calculated as follows:

$$\Delta E_k = \frac{m}{e} \times \overline{v} \times \Delta v = \frac{m}{e} \times \overline{v} \times p \tag{4}$$

4) where m is the Xe^+ ion mass. ΔE_k depends upon the velocity, therefore it increases when the fluid accelerates even if p stays unchanged.

The most probable velocity is not used here. However, its value is close to the mean velocity.

C. PPSX000 Operating Conditions

All measurements were performed in the PIVOINE-2g ground-test facility. The PPSX000 thruster was equipped with BN–SiO_2 dielectric channel walls and a carbon anode. The channel is 32 mm in length. The magnetic field is maximum at the channel exit. During the experiments campaign, the applied

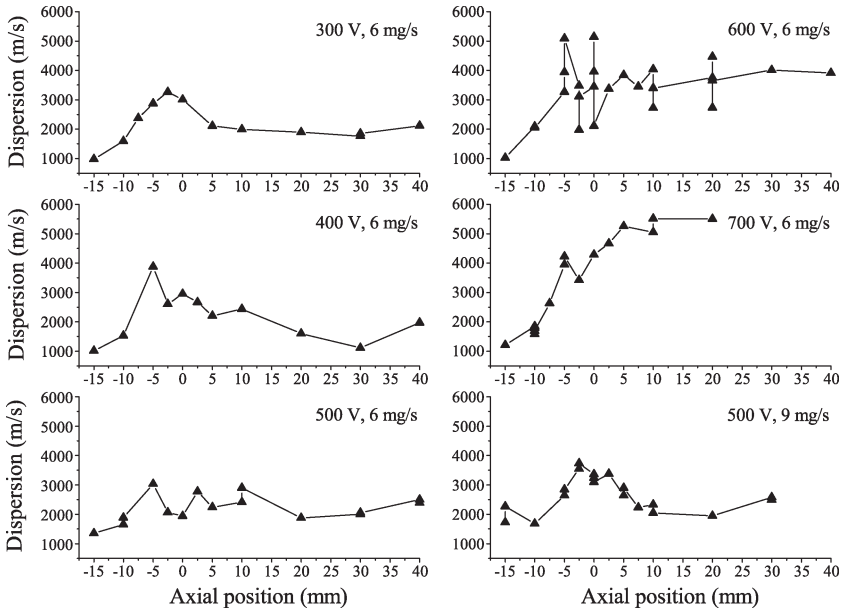

Fig. 3. Development of the Xe^+ ion axial velocity dispersion p along the channel axis for various values of U_d and Φ_a. The channel exit is at $x = 0$ mm.

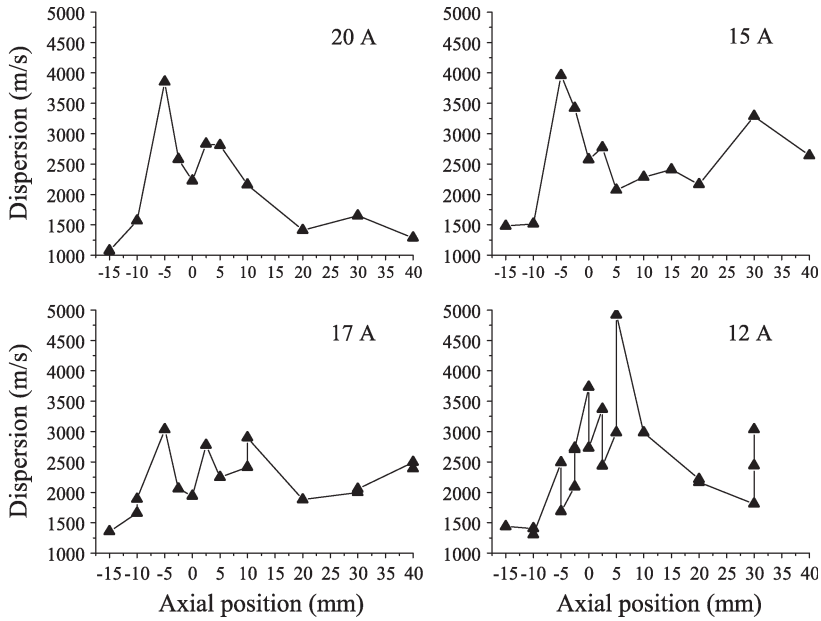

Fig. 4. Development of the Xe^+ ion axial velocity dispersion p along the channel axis for various values of I_c. The channel exit is at $x = 0$ mm.

voltage, the magnetic-field strength, and the mass flow rate have been changed is such a way that nine distinct operating conditions have been studied.

1) Voltage series ($\Phi_a = 6$ mg/s, $I_c = 17$ A): $U_d = 300$, 400, 500, 600, and 700 V.
2) Magnetic-field series ($U_d = 500$ V, $\Phi_a = 6$ mg/s): $I_c = 20$, 17, 15, and 12 A (i.e., B varies from 160 down to 100 G).
3) Mass-flow-rate series ($U_d = 500$ V, $I_c = 17$ A): $\Phi_a =$ 6 mg/s, 9 mg/s.

The xenon gas flow rate through the cathode was kept fixed at 0.6 mg/s. The power range stretched from 1500 to 4200 W. The background pressure inside the vacuum chamber was 1.4×10^{-5} mbarXe for all conditions.

IV. Ion VDF Properties

A. Velocity Dispersion

The Xe^+ ion VDF broadens along the x-direction whatever the values of U_d, B, and Φ_a. The evolution of p with U_d and Φ_a is shown in Fig. 3. Below 600 V, the dispersion in axial velocity goes through a maximum. The maximum value of p, which is around 3000–3500 m/s, is reached in the vicinity of the exit plane of the channel. At and above 600 V, the dispersion seems to reach a plateau. In fact, the maximum could be shifted

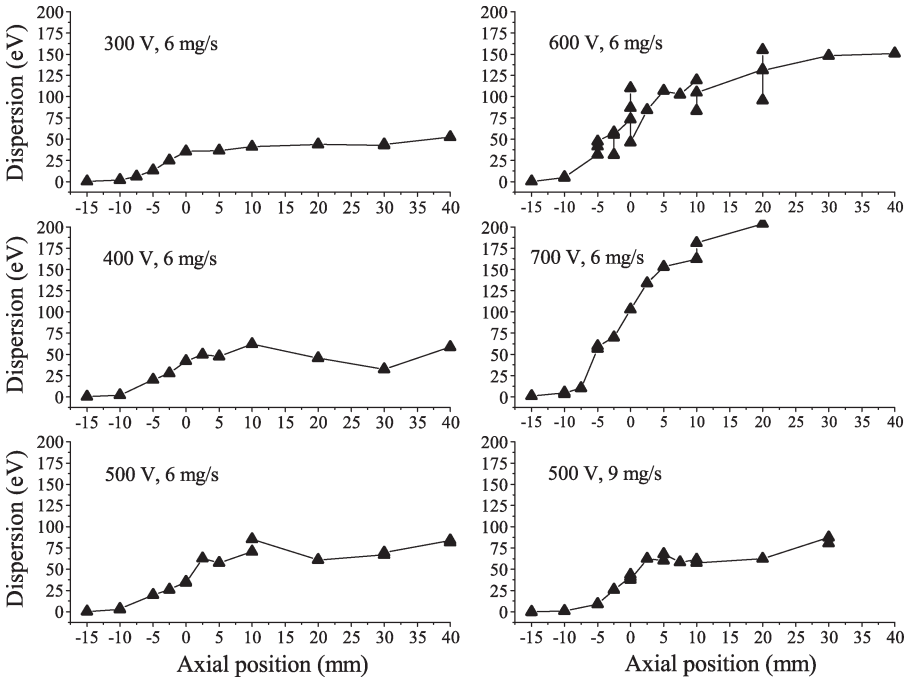

Fig. 5. Development of the spread in Xe^+ kinetic energy along the channel axis for various values of U_d and Φ_a.

downstream. As shown in Fig. 4, the magnetic-field strength does not influence much the velocity dispersion [11]; p reaches a maximum around 4000 m/s close to the channel exhaust. On the contrary, the applied voltage has a drastic impact upon the value and the profile of the dispersion. First, the dispersion increases with U_d; it reaches $\approx$ 5500 m/s at 700 V. The impact of U_d is even more obvious when considering the spread in kinetic energy. On-axis profiles of ΔE_k are shown in Fig. 5 for the voltage series. Whereas ΔE_k is around 70 eV at 500 V for all B field configurations [11], it reaches 200 eV at 700 V, i.e., 28% of the applied potential energy. Second, the shape of the profile of p and ΔE_k along the channel axis depends strongly upon the voltage. The change from a typical single-peaked curve at low voltage to a curve that tends toward a limit at high voltage may be connected with two previously reported phenomena. The thrust efficiency drops at high voltage whatever the HET design [7], as shown in Fig. 6 for the PPSX000 thruster. The development of the channel-wall temperature with the applied voltage changes suddenly above a certain value of U_d which is around 550 V for the PPSX000 thruster [7]. The observed trends may be a sign for a break in the physics at work in a HET above a certain threshold in voltage. The change could be linked to the production of multiply charged ions, to the saturation of the plasma sheath [12], [13], as well as to the EEDF properties. A large value of the Xe^+ axial velocity dispersion was also observed in the PPS100 thruster [14]. The maximum value of p was of about 4000 m/s. The behavior as a function of the input voltage U_d is identical.

The broadening of the Xe^+ ion VDF in the course of the flow and the value of the velocity dispersion and of the spread in kinetic energy are, at present, well understood. They originate in the overlap between the ionization and the acceleration layers [11], [14], [15].

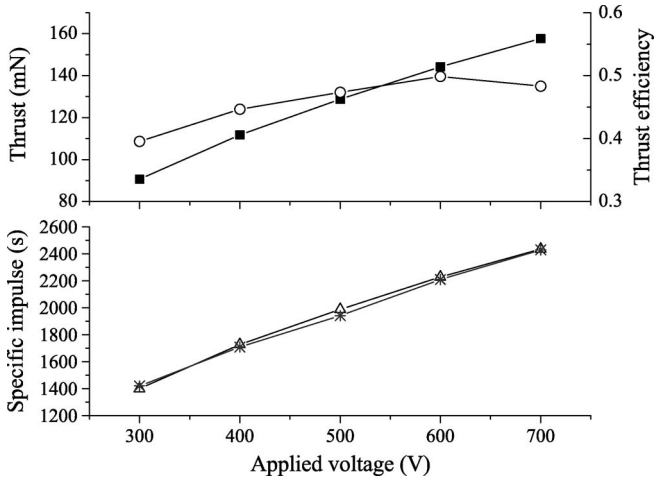

Fig. 6. Top: (square) Thrust and (circle) thrust efficiency of the PPSX000 HET as a function of the applied voltage (6 mg/s, 17 A). Bottom: Specific impulse derived from the (triangle) thrust and specific impulse computed from the mean axial ion velocity ($x = 40$ mm) assuming a 40° beam divergence angle. For 700 V, the far-field velocity was obtained from RPA measurements.

The broadening of the Xe^+ ion VDF along the channel axis in the direction of the flow is a general feature for HETs that does depend neither on the size of the thruster nor on the input power. Numerical simulations carried out with both a hybrid model [16] and a kinetic (PIC) model [17] show that the ion VDF broadening phenomenon finds its origin in the existence of a partial overlap between the ionization and the acceleration layers. Calculations carried out with a hybrid model when the electron properties are frozen indicate that the on-axis distribution of the velocity dispersion p depends strongly on both the shape and the position of the ion-source

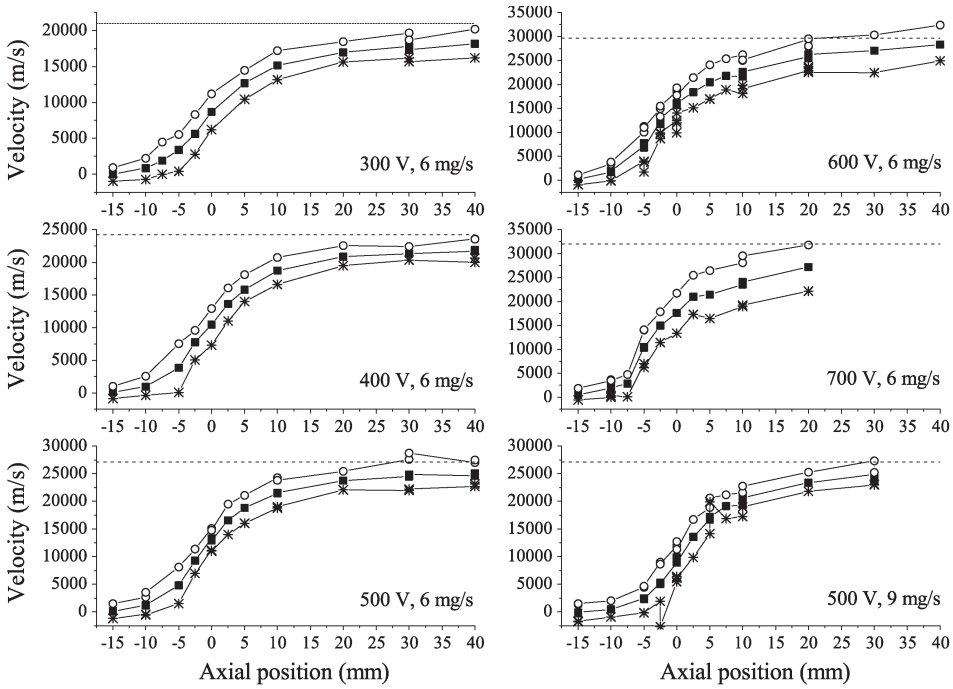

Fig. 7. Xe^+ ion axial velocity component as a function of the position along the channel axis of the PPSX000 thruster for several values of U_d and Φ_a. (Square) The mean velocity $\bar{v}$, (circle) the maximum velocity $v_{\max}$, and (star) the minimum velocity $v_{\min}$ are plotted.

term [15]. These two parameters in fact determine the degree of overlap between the two zones. Oscillations of the acceleration potential can amplify the phenomenon when they lead to an increase in the length of the overlap region. Charge-exchange collisions play a minor role in the value of p, as they are very rare in the acceleration region [14]. Computational simulations also indicate that the maximum of the velocity dispersion is reached at the end of the ionization layer. Experimental results shown in Figs. 3 and 5 can therefore be interpreted as follows. The dispersion increases and the maximum value of p is shifted downstream when U_d increases as the overlap between the ionization and acceleration zones increases with the voltage. Moreover, the plateau observed at 600 and 700 V in the dispersion profile indicates that ions are created throughout the whole acceleration region at high voltage. Such properties are likely linked to the electron temperature that rises with the applied voltage [18], [19]. Ionization is favored at high voltage, and the ion-source term extends over the channel near field.

This paper reveal that, in a HET, ionization and acceleration processes are deeply mixed up. It is therefore difficult with a classical HET design and architecture to control, in an independent manner, the thrust and the specific impulse.

B. Velocities

The evolution of the Xe^+ ion axial mean, maximum, and minimum velocities as a function of the axial position x is shown in Fig. 7 for several values of U_d and Φ_a. In Fig. 7, the dashed line correspond to the ion velocity obtained, assuming a full conversion of the potential energy $e\,U_d$ into axial kinetic energy. This velocity is often referred to as the maximum achievable velocity. The highest value of the mean ion axial velocity component is close to the theoretical limit but it always stays below. In fact, the input potential energy $e\,U_d$ is not solely converted into axial motion: A fraction is transformed into radial motion, a part contributes to ionization, and a part is used to heat up the electron gas. Moreover, voltage losses at the cathode make anyway the potential available for acceleration below the applied potential. The length of the acceleration layer is around 40 mm. Note that the measurement at 700 V is not all accomplished yet; the final ion velocity may be higher than the one shown in Fig. 7. The shape of the velocity profile depends on the applied voltage: The gradient is steeper when U_d is ramped up, and the whole profile is shifted toward the anode. The gas flow rate has a small effect on the velocity. The impact of the B field was described in a previous paper [11]. In brief, the magnetic field has a little influence on the velocity; however, the velocity profile slightly moves upstream when B increases. The same tendencies were observed with the PSS100 thruster [14].

In Fig. 6, the specific impulse $(I_{\rm sp})$ computed from the measured mean axial ion velocity is shown as a function of the applied voltage. A 40° ion-beam divergence angle is assumed in the calculation. The $I_{\rm sp}$ therefore reads

$$I_{\rm sp} = \overline{v}/g \times \cos(40^\circ) \tag{5}$$

where g is the standard gravity. As shown in Fig. 6, the computed $I_{\rm sp}$ is in good agreement with the measured one [7].

The maximum ion velocity $v_{\max}$ is often above the limit given by U_d, particularly at high voltage, as shown in Fig. 7. Therefore, there is a nonnegligible fraction of Xe^+ ions that have a kinetic energy greater than the applied potential energy. Such fast ions were also found in the far-field plasma plume of

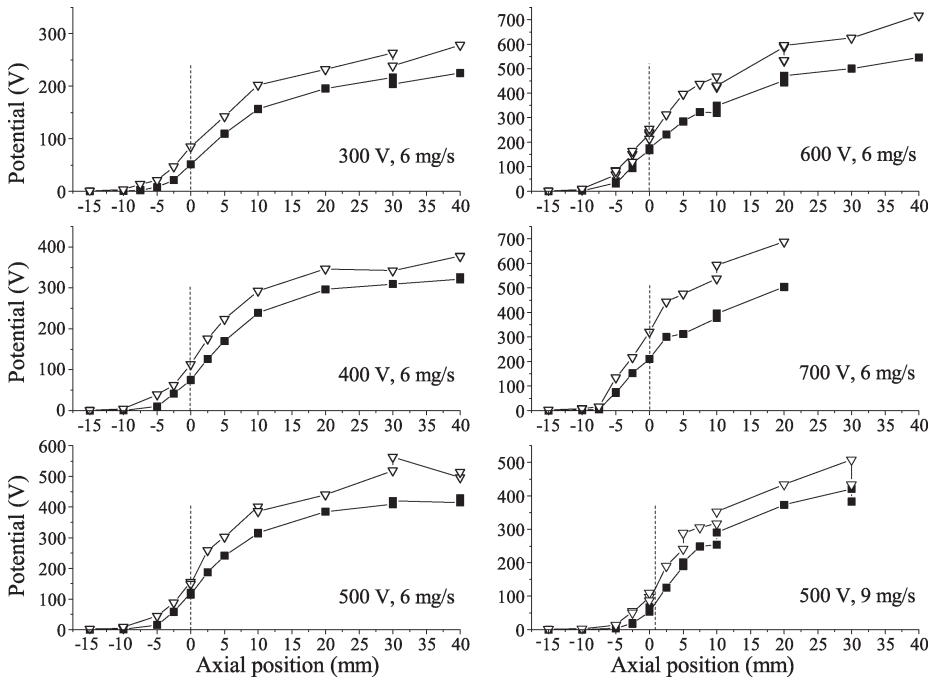

Fig. 8. Distribution of the acceleration potential along the channel axis of the PPSX000 thruster for various values of U_d and Φ_a. The potential curve is derived from (square) the mean velocity and (triangle) the maximum velocity.

the PPS100 thruster by means of retarding potential analyzer (RPA) [10] and mass spectrometer [20]. Moreover, they were detected by LIF spectroscopy in the near plume of the low-power BHT-200-X3 Hall thruster [21]. The fraction of very fast ions seems to increase with U_d. The origin of fast ions is not yet clear. Charge-exchange process between atom and/or Xe^+ ions and multiply charged ions like Xe^{2+} and Xe^{3+} is a possible explanation. Xe^+ ions could also acquire a very large speed due to oscillations of the electric field in space and in time. As a counterpart of fast ions, very slow ions are always observed in the plasma of a HET [10], [21]. The on-axis profile of $v_{\min}$ is shown in Fig. 7. Computer simulations with a hybrid code suggest that oscillations of the electric field are at the origin of the production of very slow ions ($E_k \ll e\,U_d$) and very fast ions ($E_k \gg e\,U_d$) [22]. PIC simulations predict as well the existence of very fast and very slow ions, whereas charge-exchange mechanisms are not included into the model [17]. Recent calculations carried out by our team confirm this assumption. A kinetic model with a fixed ionization region and a constant source term unambiguously show that oscillations in time of the electric field with frequencies that correspond to the reciprocal of the Xe^+ ion transit time across the acceleration layer ($f = 100$ kHz-1 MHz) generate fast and slow Xe^+ ion. Besides, the average kinetic energy of the ion fluid always stays below the applied potential.

V. Acceleration Potential and Electric Field

The acceleration potential $U_{\rm acc}$ is calculated according to the formula

$$\frac{1}{2}mv^2 = e\,U_{\rm acc} \tag{6}$$

where v is either the mean velocity $\bar{v}$ or the so-called maximum velocity $v_{\max}$. Acceleration potential profiles along the channel axis are shown in Fig. 8 for various voltages and propellant mass flow rates. As a nonnegligible amount of Xe^+ ions are created within the acceleration layer, the acceleration potential computed from $\bar{v}$ is underestimated [14]. Moreover, the gap between the "true" potential and the calculated one increases with U_d as the overlap between the ionization and acceleration layers increases with U_d. Therefore, the use of $v_{\max}$ instead of $\bar{v}$ provides a more realistic value of the local potential as the fastest ions necessarily experience the full potential drop. However, when the effect of electric-field oscillations is not negligible, the fastest ions can gain more than the applied potential, as previously discussed. Thus, another reason to discard 10% of the most rapid ions (see the definition of $v_{\max}$) is to attenuate the effect of oscillations on the estimation of the acceleration potential. A correct estimate of the potential profile is not obvious, as it strongly depends upon processes accounted for. However, we believe that the potential assessed from $v_{\max}$ is the most appropriated.

Table I shows the fraction of accelerating potential inside the thruster channel $\Delta U_{\rm in}$ calculated as follows:

$$\Delta U_{\rm in} = \frac{U_{\rm acc}|_{x=0}}{U_d}. \tag{7}$$

Numbers given in Table I indicate that the choice of either $\bar{v}$ or $v_{\max}$ to compute $U_{\rm acc}$ impacts greatly onto the value of $\Delta U_{\rm in}$. As shown in Fig. 8 and in Table I, most of the acceleration occurs outside the channel whatever the operating parameters. The potential gradient becomes steeper when U_d rises. The potential moves upstream with an increasing U_d and downstream with a growing Φ_a, as shown in Fig. 8. In other

TABLE I
EVOLUTION OF THE FRACTION OF THE ACCELERATING POTENTIAL INSIDE THE THRUSTER CHANNEL FOR VARIOUS PPSX000 THRUSTER OPERATING PARAMETERS. THE SUPERSCRIPT *mean*, RESPECTIVELY *max*, REFERS TO THE MEAN ION VELOCITY, RESPECTIVELY TO THE MAXIMUM ION VELOCITY

Change of U_d (ϕ_a = 6 mg/s, I_c = 17 A)			Change of B (ϕ_a = 6 mg/s, U_d = 500 V)		
U_d (V)	ΔU_{in}^{mean}	ΔU_{in}^{max}	I_c (A)	ΔU_{in}^{mean}	ΔU_{in}^{max}
300	0.17	0.28	12	0.15	0.23
400	0.18	0.28	15	0.24	0.32
500	0.23	0.30	17	0.23	0.30
600	0.29	0.34	20	0.21	0.28
700	0.30	0.46			

words, the part of the acceleration potential located inside the channel increases with U_d and decreases with Φ_a. As shown in Table I, the percentage of potential inside the channel increases from 0.28% to 0.46% when U_d varies from 300 to 700 V. The magnetic field has a little impact on the potential, however, the fraction of the potential located inside the channel increases a bit with I_c. Notice that, with the PPS100 Hall thruster, the effect of the magnetic field is much more pronounced. For the 9-mg/s case, one find $\Delta U_{\rm in}^{\rm mean} = 0.12$ and $\Delta U_{\rm in}^{\rm max} = 0.20$. When the propellant mass flow rate is ramped up, the potential profile moves downstream. In all cases, a large fraction of the potential drop, i.e., $\approx$ 60%–70%, is located outside the channel. A similar remark holds for the PPS100 thruster.

The electric field in axial direction E_x is the derivative of the acceleration potential

$$|E_x(x)| = \frac{dU_{\rm acc}(x)}{dx} = \frac{m}{e} v(x) \frac{dv(x)}{dx}. \tag{8}$$

In order to numerically compute E_x, it is necessary to smooth the potential profile and to interpolate the resulting curve using, e.g., cubic splines. The shape of E_x is quite sensitive to the data-treatment procedure. The electric-field distribution along the channel axis is shown in Fig. 9 for all operating conditions. In this figure, the electric field is calculated from the Xe^+ maximum velocity profile to filter out the effect of slow ions. The electric field obtained from the mean velocity can be found in [11] and [15]. The magnitude and the shape of the E_x field depend upon the chosen velocity as expected. On the contrary, the change of the electric field with the operating conditions is not influenced by the selection of $\bar{v}$ or $v_{\rm max}$.

As shown in Fig. 9, the magnitude of E_x increases with U_d, and the maximum of the field is shifted upstream when U_d is ramped up. Linnel and Gallimore [19] observed identical trends with the high-power 173Mv1 Hall thruster from NASA, although they found a stronger field. On the channel centerline, E_x reaches up to 420 V/cm at 300 V and 700 V/cm at 500 V with a trim coil (TC). In these experiments, the axial electric field was inferred from emissive probe measurements. With the PPSX000 thruster, a large part of the electric-field profile is located outside the channel whatever the voltage. Moreover, the width of the electric field on-axis distribution narrows down

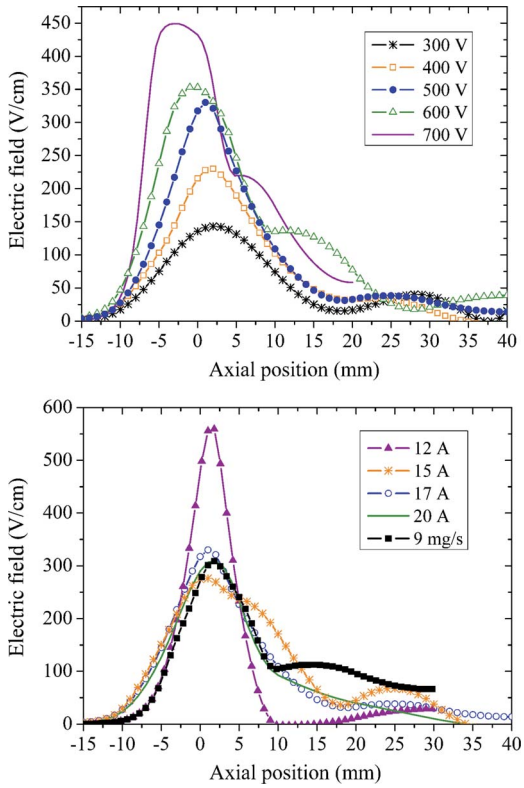

Fig. 9. On-axis development of the PPSX000 thruster acceleration electric field E_x as a function (top) of applied voltage, (bottom) coil current, and (bottom) gas flow rate. The electric field is computed from the maximum ion velocity $v_{\rm max}$.

TABLE II
AVERAGED ELECTRIC FIELD $\bar{E}_x$ (IN VOLTS PER CENTIMETER) AND SPATIAL EXTENT OF THE ELECTRIC FIELD δE_x (IN CENTIMETERS) FOR VARIOUS OPERATING CONDITIONS WHEN E_x IS OBTAINED FROM THE $v_{\rm max}$ DATA SET

Change of U_d (ϕ_a = 6 mg/s, I_c = 17 A)			Change of B (ϕ_a = 6 mg/s, U_d = 500 V)		
U_d (V)	$\bar{E}$	δE	I_c (A)	$\bar{E}$	δE
300	71	4.2	12	183	2.7
400	100	4.0	15	142	3.5
500	130	3.8	17	130	3.8
600	191	3.1	20	145	3.5
700	198	3.5			

when U_d increases, i.e., the length of the acceleration layer decreases when U_d rises. Table II contains the value of the mean field $\bar{E}_x$ within the acceleration zone and of the quantity δE_x that characterizes the expansion of the field. The quantity δE_x is the ratio of U_d to $\bar{E}_x$. It is clear that $\bar{E}_x$ increases with U_d, whereas δE_x decreases with U_d. The acceleration electric-field properties and development with the applied voltage are found to be similar for the SPT100 thruster [10]. The increase of the electron kinetic energy with the applied voltage could explain the measurement outcomes [14]. At high voltage, electrons are not efficiently confined as the Larmor radius increases. They penetrate deeper into the magnetic field, hence, the electric field shifts toward the anode. They are

trapped over a shorter distance, hence, a narrower electric-field distribution.

Changing the magnetic field does not affect much the electric field in the case of the PPSX000 thruster except when the B field is weak, see Fig. 9. As shown in Table II, the two quantities $\bar{E}_x$ and δE_x do not vary much with I_c. With the PPS100 Hall thruster, the effect of the magnetic field is much more pronounced: At low magnetic-field strength, E_x is entirely outside the channel, and it moves upstream when I_c is increased.

When the gas flow rate mounts, the electric-field distribution moves downstream but its shape is not modified, see Fig. 9. In the 9-mg/s case, one finds $\bar{E}_x = 132$ V/cm and $\delta E_x = 3.8$ cm, i.e., the same values as in the 6-mg/s case.

This paper also reveals that, whatever the operating conditions, a part of the ionization process occurs in a region of strong electric field, particularly at high voltage, which is a weak point for HET in terms of performance level.

The length of the acceleration region is typically around 30–40 mm for both the PPSX000 and the PPS100 thrusters. Moreover, a large fraction of the acceleration potential, of about 60%–70%, is located outside the channel. For a standard HET, the acceleration electric field is always localized within a narrow area in the vicinity of the channel exhaust. However, the exact properties of the acceleration layer depend upon the operating conditions and the architecture of the thruster, particularly upon the magnetic-field map. In the case of the 173Mv1 Hall thruster, the length of the acceleration region is around 30 mm, and the fraction of potential outside the channel varies from 54% at 300 V up to 44% at 500 V for TC conditions when assuming that the plasma potential matches the acceleration potential [19]. For the low-power Standford Hall thruster fired at 200 V, the size of the acceleration region is of about 40–50 mm, and ions experience 45% of the acceleration potential beyond the channel exit plane [23]. For the sake of clarity, the potential fraction is always computed with (7).

VI. Conclusion

LIF spectroscopy studies on the time-averaged Xe^+ ion VDF performed with the PPSX000 and the PPS100 HETs show the impact of the applied voltage, the magnetic field, the xenon mass flow rate, and the thruster dimensions on kinetic-energy spread and acceleration electric-field profile. This paper also provides information about the overlap between the ionization and the acceleration layers. Moreover, they reveal the existence of very slow and very fast ions of which the origin is still not established. However, as suggested by numerical-simulation outcomes, oscillation of the electric field in space and in time could be an explanation.

References

[1] M. Martinez-Sanchez and J. E. Pollard, "Spacecraft electric propulsion—An overview," *J. Propuls. Power*, vol. 14, no. 5, pp. 688–699, Sep./Oct. 1998.

[2] R. H. Frisbee, "Advanced space propulsion for the 21st century," *J. Propuls. Power*, vol. 19, no. 6, pp. 1129–1154, 2003.

[3] C. R. Koppel, F. Marchandise, M. Prioul, D. Estublier, and F. Darnon, "The SMART-1 electric propulsion subsystem around the Moon: In flight experience," presented at the 41st AIAA/ASME/SAE/ASEE Joint Propulsion Conf. and Exhibit, Tucson, AZ, 2005, AIAA Paper 05-3671.

[4] A. I. Morozov and V. V. Savelyev, "Fundamentals of stationary plasma thruster theory," in *Reviews of Plasma Physics*, vol. 21, B. B. Kadomtsev and V. D. Shafranov, Eds. New York: Consultants Bureau, 2000, pp. 203–391.

[5] V. V. Zhurin, H. R. Kaufman, and R. S. Robinson, "Physics of closed drift thrusters," *Plasma Sources Sci. Technol.*, vol. 8, no. 1, pp. R1–R20, Feb. 1999.

[6] N. Gascon, M. Dudeck, and S. Barral, "Wall material effects in stationary plasma thrusters. I. Parametric studies of an SPT-100," *Phys. Plasmas*, vol. 10, no. 10, pp. 4123–4136, Oct. 2003.

[7] S. Mazouffre, A. Lazurenko, P. Lasgorceix, M. Dudeck, S. d'Escrivan, and O. Duchemin, "Expanding frontiers: Towards high power Hall effect thrusters for interplanetary journeys," presented at the 7th International Symp. on Launcher Technologies, Barcelona, Spain, 2007, Paper O-25.

[8] W. A. Hargus, Jr. and M. A. Cappelli, "Laser-induced fluorescence measurements of velocity within a Hall discharge," *Appl. Phys. B, Photophys. Laser Chem.*, vol. 72, p. 961, 2001.

[9] N. Dorval, J. Bonnet, J. P. Marque, E. Rosencher, S. Chable, F. Rogier, and P. Lasgorceix, "Determination of the ionization and acceleration zones in a stationary plasma thruster by optical spectroscopy study: Experiments and model," *J. Appl. Phys.*, vol. 91, no. 8, p. 4811, 2002.

[10] D. Gawron, S. Mazouffre, L. Albarède, and N. Sadeghi, "Examination of Hall effect thruster acceleration layer characteristics by laser spectroscopy and retarding potential analyzer," presented at the 42nd AIAA/ASME/SAE/ASEE Joint Propulsion Conf. and Exhibit, Sacramento, CA, 2006, AIAA Paper 06-4473.

[11] S. Mazouffre, D. Gawron, V. Kulaev, and N. Sadeghi, "A laser spectroscopic study on Xe^+ ion transport phenomena in a 5 kW-class Hall effect thruster," presented at the 30th International Electric Propulsion Conf., Florence, Italy, 2007, Paper 160.

[12] S. Barral, K. Makowski, Z. Peradzyñski, N. Gascon, and M. Dudeck, "Wall material effects in stationary plasma thrusters. II. Near-wall and in-wall conductivity," *Phys. Plasmas*, vol. 10, no. 10, pp. 4137–4152, Oct. 2003.

[13] E. Ahedo, J. M. Gallardo, and M. Martinez-Sanchez, "Effects of the radial plasma–wall interaction on the Hall thruster discharge," *Phys. Plasmas*, vol. 10, no. 8, pp. 3397–3409, 2003.

[14] D. Gawron, S. Mazouffre, N. Sadeghi, and A. Héron, "Influence of magnetic field and discharge voltage on the acceleration layer features in a Hall effect thruster," *Plasma Sources Sci. Technol.*, vol. 17, no. 2, pp. 025 001–025 010, May 2008.

[15] S. Mazouffre, D. Gawron, V. Kulaev, J. Pérez Luna, and N. Sadeghi, "A laser spectroscopic study on Xe^+ ion transport phenomena in the $E \times B$ discharge of a Hall effect thruster," in *Proc. Int. Conf. Res. Appl. Plasmas*, Greisfswald, Germany, 2007. to be published in the series of AIP conference proceedings.

[16] J. Bareilles, G. J. M. Hagelaar, L. Garrigues, C. Boniface, J. P. Boeuf, and N. Gascon, "Critical assessment of a two-dimensional hybrid Hall thruster model: Comparisons with experiments," *Phys. Plasmas*, vol. 11, no. 6, p. 3035, May 2004.

[17] J. C. Adam, A. Héron, and G. Laval, "Study of stationary plasma thrusters using two-dimensional fully kinetic simulations," *Phys. Plasmas*, vol. 11, no. 1, p. 295, Jan. 2004.

[18] Y. Raitses, D. Staack, M. Keidar, and N. J. Fisch, "Electron–wall interaction in Hall thrusters," *Phys. Plasmas*, vol. 12, no. 5, p. 057 104, May 2005.

[19] J. A. Linnell and A. D. Gallimore, "Internal plasma potential measurements of a Hall thruster using plasma lens focusing," *Phys. Plasmas*, vol. 13, no. 10, p. 103 504, Oct. 2006.

[20] L. B. King and A. D. Gallimore, "Ion-energy diagnostics in an SPT-100 plume from thrust axis to backflow," *J. Propuls. Power*, vol. 20, no. 2, pp. 228–242, 2004.

[21] W. A. Hargus, Jr. and M. R. Nakles, "Evolution of the ion velocity distribution in the near field of the BHT-200-X3 Hall thruster," presented at the 42nd AIAA/ASME/SAE/ASEE Joint Propulsion Conf. and Exhibit, Sacramento, CA, 2006, AIAA Paper 06-4991.

[22] G. J. M. Hagelaar, J. Bareilles, L. Garrigues, and J.-P. Boeuf, "Role of anomalous electron transport in a stationary plasma thruster simulation," *J. Appl. Phys.*, vol. 93, no. 1, p. 67, Jan. 2003.

[23] M. K. Scharfe, N. Gascon, M. A. Cappelli, and E. Fernandez, "Comparison of hybrid Hall thruster model to experimental measurements," *Phys. Plasmas*, vol. 13, no. 8, pp. 083 505-1–083 505-12, Aug. 2006.

Stéphane Mazouffre was born in Limoges, France, in 1973. He received the M.Sc. degree in materials science and surface treatments from ENSIL–University of Limoges, Limoges, France, in 1996 and the Ph.D. degree (*summa cum laude*) in plasma physics from Eindhoven University of Technology, Eindhoven, The Netherlands, in 2001.

Since 2002, he has been a Postdoctoral Fellow working in the field of rarefied supersonic plasma jets with the CARE Institute, Orléans, France, where he is currently a CNRS Research Scientist and leads the Electric Propulsion Team. His research interest includes low-pressure discharges for space applications and plasma diagnostics (particularly laser spectroscopy).

Dr. Mazouffre is a member of the French joint-research program 2759 "Propulsion Spatiale à Plasma."

Damien Gawron was born in Reims, France, in 1980. He received the M.Sc. degree in optical, laser, and plasma processes from Polytech'Orléans, Orléans, France in 2004, and the Ph.D. degree in plasma physics in the field of electric propulsion with the CARE Institute, Orléans, France, in 2007.

Vladimir Kulaev was born in Nalchik, former USSR, in 1984. He received the B.Sc. degree from the Faculty of Power Engineering, Department of Plasma Power Plants, Bauman Technical University, Moscow, Russia, and the M.Sc. degree in aeronautics and space technology from the University of Pisa, Pisa, Italy, and Supaero, Toulouse, France. He has been working toward the Ph.D. degree with the Electric Propulsion Team at the CARE Institute, Orléans, France, since 2007.

He first worked with the electric thrusters in the Department of Plasma Power Plants, Bauman Technical University. He is actively involved with research on transport phenomena and electron properties in Hall thrusters.

Nader Sadeghi received the M.S. degree in physics and the Doctorat d'Etat es Science Physique for his work on "Kinetics of metastable atoms and charged particles in argon afterglow," from the University of Grenoble, Grenoble, France, in 1964 and 1974, respectively.

In 1965, he was an Assistant Professor with the University of Grenoble. Since 1969, he has been with the Centre National de la Recherche Scientifique (CNRS), where he is currently the Director of Research Emeritus in Laboratoire de Spectrométrie Physique, a joint institute of CNRS and the University of Grenoble. He is the Founder of the Plasma and Reactive Collisions Group, Grenoble University. He was an Invited Professor, or Associated Researcher, in different universities abroad such as KSU, USA; NDA, Japan; TUE, The Netherlands; Nagoya, Japan; and a Consulting Scientist for AT&T Bell Laboratories, Murry Hill, NJ, and Centre National d'Etude des Télécommunications, France. His current interests include plasma diagnostics, plasma chemistry, plasma processing, optical spectroscopy, and collisional processes.